energy&fuels

pubs.acs.org/EF

Article

Constructing a Crystalline $NiCo_2O_4$/Amorphous NiFeO(OH) Heterostructure for Boosting Electrocatalytic Water Oxidation

Jia Heng Leng, Zeng Guo Wang, Xiaoxia Li, Zhaoliang Wang, Xin Yu Zhang,* Ji Kai Liu, Peng Fei Liu,* and Hua Gui Yang

Cite This: *Energy Fuels* 2025, 39, 17522−17530

Read Online

ACCESS | Metrics & More | Article Recommendations | Supporting Information

ABSTRACT: The construction of efficient oxygen evolution reaction (OER) electrocatalysts is significant in enhancing the efficiency of electrocatalytic hydrogen production. Heterostructure amorphous−crystalline materials have advantages with good conductivity and increased exposure to active sites. They have also been developed as prospective OER catalysts in an alkaline medium. This study synthesized an amorphous−crystalline composite heterostructure catalyst, $NiCo_2O_4$@a-NiFeO(OH), via a simple hydrothermal and impregnation treatment. Structural characterizations indicated that the $NiCo_2O_4$ scaffold exerts a crucial function in determining the morphology of amorphous NiFeO(OH). The catalyst demonstrated outstanding OER activity, requiring overpotentials of only 219.6 mV and 260.8 mV at current densities of 10 mA cm^{-2} and 100 mA cm^{-2}, respectively. The enhanced OER performance is attributed to the synergistic electronic interactions within the heterostructure, combined with increased surface hydroxylation, which identifies Ni species as the key active sites for the OER. This study underscores the potential of heterostructure design in advancing electrocatalytic OER performance.

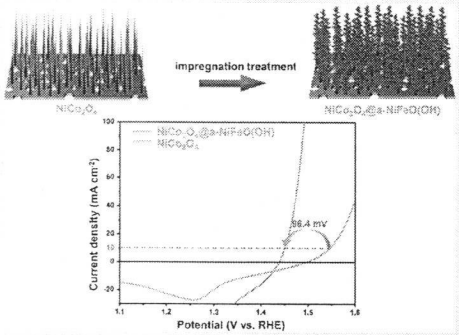

1. INTRODUCTION

The prevailing reliance on fossil fuels as the principal energy source poses a significant risk of impending energy crises and environmental challenges, exacerbated by the growing global population and increasing energy demands.[1,2] Hydrogen fuel emerges as an ideal zero-emission alternative due to its abundant sources and excellent calorific properties.[3,4] Electrochemical water splitting is an efficient and environmentally friendly way to produce high-purity hydrogen, capitalizing on its ability to convert electrical energy into hydrogen and oxygen gases via the hydrogen evolution reaction (HER) and oxygen evolution reaction (OER).[5,6] However, both the HER and the OER are impeded by slow mass and charge transfer kinetics. Particularly, OER, as a four-electron transfer process, encounters substantial energy barriers, thereby acting as a critical bottleneck in the overall water electrolysis reaction.[7−9] To tackle this challenge, the rational design of efficient and stable OER catalysts is thus increasingly crucial in promoting energy conversion technologies.[10]

Nickel-based materials have garnered attention for their superior OER electrocatalytic activity and stability in alkaline environments, making them prominent candidates for alkaline water electrolysis.[11−13] Recently, nickel-based catalysts such as NiMn, NiCo, and NiFe have shown significant promise in this regard.[14,15] Specifically, nickel-based oxides and hydroxides have been extensively investigated and utilized as OER catalysts in alkaline media.[16,17] These highly active electrocatalysts can efficiently decrease the energy barrier and the overpotential needed for the reaction. As a result, they can greatly accelerate the electrochemical processes on the electrode surface and enhance the overall efficiency of the water electrolysis reaction.[18,19]

It is worth noting that the construction of composite heterostructures through interfacial engineering has demonstrated significant potential in enhancing the physicochemical properties of electrocatalytic materials.[20−22] The formation of heterogeneous interfaces generally gives rise to remarkable synergistic effects and electronic interactions. These can augment active site exposure and improve the catalysts' overall electrochemical performance.[23,24] In addition, such heterogeneous structures can optimize the binding energy of adsorbed intermediates during water electrolysis, thereby lowering the energy barriers associated with HER and OER.[25,26] Recent research has rapidly shifted focus toward composite materials combining amorphous and crystalline phases to form heterostructures.[27,28] This combination combines the excellent electrical conductivity of the crystalline phase and the

Received: May 22, 2025
Revised: August 18, 2025
Accepted: August 22, 2025
Published: August 29, 2025

https://doi.org/10.1021/acs.energyfuels.5c02583
Energy Fuels 2025, 39, 17522−17530

structural disorder of the amorphous phase, potentially including synergistic effects and enhancing catalytic performance.[29,30] For instance, Yang et al. developed crystalline $Ni_{0.70}Fe_{0.10}V_{0.20}$@amorphous NiFe hydroxide composite heterostructures. These heterostructures exhibited outstanding OER performance, having an overpotential as low as 204 mV when the current density is 10 mA cm^{-2} (η_{10} = 204 mV).[31] This high catalytic activity is attributed not only to the inherent OER activity of the amorphous NiFe hydroxides but also to the synergistic impacts between the core and shell components, the high electronic conductivity of the core, and the abundant catalytically active sites on the amorphous shell. Similarly, Gong et al. reported the a/c-NiFe-G with an amorphous−crystalline heterogeneous phase, which showed enhanced OER performance with the η_{10} of merely 250 mV.[32] The superior OER performance was attributed to the unsaturated coordination configuration and abundant amorphous−crystalline interfaces.

Herein, an amorphous−crystalline composite heterostructure catalyst ($NiCo_2O_4$@a-NiFeO(OH)) was synthesized through a straightforward hydrothermal and impregnation treatment. This catalyst showed remarkable OER activity, with overpotentials of merely 219.6 mV and 260.8 mV at current densities of 10 mA cm^{-2} and 100 mA cm^{-2}, respectively. The $NiCo_2O_4$ scaffold was found to influence the morphology of amorphous NiFeO(OH), as revealed by various characterizations. The synergistic and electronic interactions within the heterostructure, coupled with enhanced hydroxylation of the sample surface, collectively enhance the OER performance, as evidenced by X-ray Photoelectron Spectroscopy (XPS) characterization of Ni species, which are identified as the primary active sites.

2. EXPERIMENTAL SECTION

2.1. Materials and Chemicals. Nickel chloride hexahydrate ($NiCl_2·6H_2O$, 98.0%), cobalt chloride hexahydrate ($CoCl_2·6H_2O$, 99.0%), manganese chloride hexahydrate ($MnCl_2·6H_2O$, 99.0%), and ferric chloride hexahydrate ($FeCl_3·6H_2O$, 99.0%) were purchased from Sinopharm Chemical Reagent Co. Potassium hydroxide (KOH, 85.0%) was purchased from Shanghai Lingfeng Chemical Reagent Co. Ethanol (C_2H_5OH, 99.7%) and urea (CH_4N_2O, 99.5%) were purchased from Shanghai Titan Technology Co. All chemicals were used without further purification, and the Millipore system purified all water used for synthesis and analysis to >18.2 MΩ cm. Nickel foam (NF, thickness: 1.6 mm, bulk density: 0.23 g cm^{-3}) was purchased from Heze Tianyu Technology Development Co.

2.2. Catalyst Preparation. Synthesis of a Ni−Co-based precursor. All chemicals used in the experiments were of analytical grade and were not further purified. The prepared $NiCo_2O_4$ was grown on nickel foam (NF) substrates, which must be pretreated before synthesis. The NF was cut into a 2 × 4 cm^2 size, placed in acetone, and sonicated for 15 min to remove the surface oil. Subsequently, the acetone-treated NF was washed with anhydrous ethanol by placing the NF in anhydrous ethanol and ultrasonicated for 15 min, and then the above NF was transferred to a 3 M HCl solution and ultrasonicated for 15 min to remove the surface oxide layer. Finally, the NF was washed with anhydrous ethanol until the cleaning solution was clarified and free of green color; a single wash may not be able to clean the NF, and it can be cleaned several times until the cleaning solution is clarified. $NiCo_2O_4$ was prepared as follows: first, 5 mmol of $NiCl_2·6H_2O$, 2.5 mmol of $CoCl_2·6H_2O$, and 9 mmol of urea were dispersed uniformly in 32 mL of deionized water and stirred for 30 min until a clarified solution was formed, and then the solution was stirred for 30 min. The solution was stirred for 30 min until a clarified solution was formed, which was pink in color. Next, the above solution was transferred to a PTFE-lined stainless steel hydrothermal kettle with a capacity of 100 mL, and the pretreated NF was placed vertically into the kettle. Subsequently, the sample was held at 130 °C for 6 h. After it was naturally cooled to room temperature, the NF grown with Ni−Co hydrothermally was removed and washed several times with deionized water and anhydrous ethanol to remove impurities. It was then transferred to a vacuum-drying oven for overnight drying. Finally, the dried samples were placed in a muffle furnace and held at 350 °C for 2 h. The $NiCo_2O_4$ loaded on the NF was obtained after natural cooling.

Synthesis of $NiCo_2O_4$@a-NiFeO(OH): $FeCl_3·6H_2O$ and $NiCl_2·6H_2O$ were mixed in a ratio of 1:1 to form a mixed solution with a concentration of 50 mM and a total volume of 20 mL. Subsequently, the previously prepared NF loaded with $NiCo_2O_4$ was placed into this NiFe mixture for impregnation, and the impregnation time was 10 min. After that, the impregnated NF loaded with $NiCo_2O_4$ was left to dry naturally on a porcelain ark. After the sample was dried, it was repeatedly washed with deionized water and anhydrous ethanol to remove the residual Ni and Fe ions. Subsequently, the sample was placed in a vacuum drying oven at 60 °C for drying to obtain the target sample $NiCo_2O_4$@a-NiFeO(OH).

Synthesis of $NiCo_2O_4$@a-NiCoO(OH): $NiCo_2O_4$@a-NiCoO(OH) was prepared in the same steps as $NiCo_2O_4$@a-NiFeO(OH), with the difference that $FeCl_3·6H_2O$ in the impregnating solution needed to be replaced with $CoCl_2·6H_2O$.

Synthesis of $NiCo_2O_4$@a-NiMnO(OH): $NiCo_2O_4$@a-NiMnO(OH) was prepared in the same steps as $NiCo_2O_4$@a-NiFeO(OH), with the difference that $FeCl_3·6H_2O$ in the impregnating solution needed to be replaced with $MnCl_2·6H_2O$.

Synthesis of NiFe-NF, NiCo-NF, and NiMn-NF: The NiFe-NF, NiCo-NF, and NiMn-NF preparation steps are the same as those for $NiCo_2O_4$@-NiFeO(OH), with the difference being that the $NiCo_2O_4$-loaded NF is replaced with a blank NF, and the blank NF is immersed in an impregnation solution containing the corresponding metal ions.

2.3. Materials Characterizations. The corresponding crystal structure was characterized by X-ray diffraction (XRD) (D/max2550 V), and scanning transmission electron microscopy (STEM) and transmission electron microscopy (TEM) characterizations were performed using a ThermoFisher Talos F200X. HAADF-STEM images were recorded using a convergence semiangle of 11 mrad and inner and outer collection angles of 59 and 200 mrad, respectively. Energy-dispersive spectrometry (EDS) was performed using four in-column Super-X detectors. The chemical states of the elements were examined by XPS (Kratos Axis Ultra DLD). The molecular structure of the material was examined by Fourier transform infrared spectroscopy (FTIR, Nicolet iS10).

2.4. Electrochemical Evaluation on $NiCo_2O_4$@a-NiFeO(OH), $NiCo_2O_4$@a-NiCoO(OH), and $NiCo_2O_4$@a-NiMnO(OH). All electrochemical studies were carried out on an electrochemical bench (CHI 760E) in a three-electrode chamber with catalyst-decorated NF as the working electrode, a Ag/AgCl/3.5 M KCl electrode as the reference electrode, and a platinum mesh as the counter electrode. The Ag/AgCl/3.5 M KCl reference electrode was calibrated according to the reversible hydrogen electrode (RHE). The same Pt mesh was used for both the working and counter electrodes, while the Ag/AgCl (3.5 M KCl) electrode to be calibrated was selected for the reference electrode, and the electrolyte used during calibration was a 1.0 M KOH solution with a conventional type of electrolytic cell. During the calibration process, hydrogen was first passed into the electrolytic cell consisting of the above materials until saturation, and then several cyclic voltammetry (CV) tests were performed at a scan rate of 1 mV s^{-1}. After the CV curve was stabilized, the two potential values at the point where the current passed through zero were recorded, and the average value was determined as the thermodynamic potential of this reference electrode concerning the RHE. High-purity oxygen (99.999%) was continuously passed into the electrolyte for 30 min before electrochemical testing to ensure that the dissolved oxygen concentration was saturated. The electrolyzer used for the test was a conventional H-type cell, and the test environment was a 1 M KOH electrolyte. The OER performance of the prepared electrodes was evaluated by testing the voltammetric polarization curves (LSV)

https://doi.org/10.1021/acs.energyfuels.5c02583
Energy Fuels 2025, 39, 17522−17530

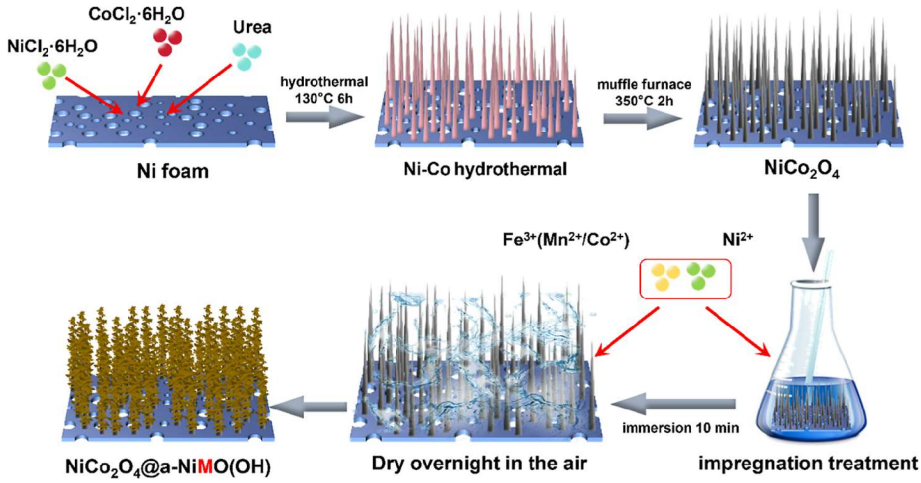

Figure 1. Schematic illustration of the synthetic approach for the $NiCo_2O_4$@a-NiMO(OH) (M = Fe, Co, Mn) heterogeneous structure on Ni foam.

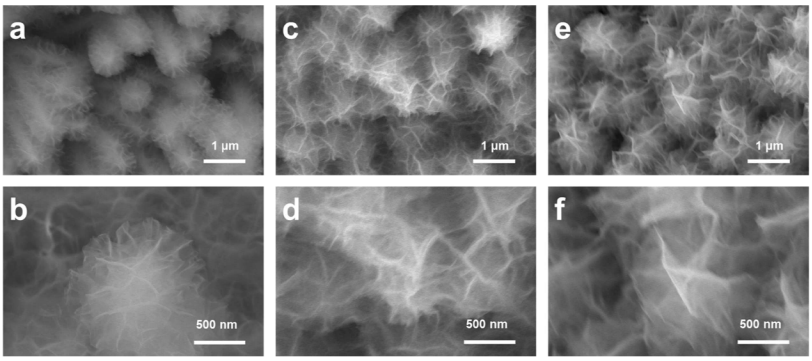

Figure 2. SEM images of (a,b) $NiCo_2O_4$@a-NiFeO(OH), (c,d) $NiCo_2O_4$@a-NiCoO(OH), and (e,f) $NiCo_2O_4$@a-NiMnO(OH) heterogeneous structures on Ni foam at different magnifications.

and CV of the materials in the potential interval of 0.8−0 V (vs Ag/AgCl), at a scan rate of 5 mV s^{-1}. During the data processing, in order to provide effective *iR* compensation and avoid excessive compensation, the LSVs of both the sample and the comparison samples were treated with 85% *iR* compensation. Electrochemical Impedance Spectroscopy (EIS) measurements were performed at a fixed overpotential (η = 0.45 V vs Ag/AgCl), corresponding to the potential required for $NiCo_2O_4$@a-NiFeO(OH) to achieve a current density of 10 mA cm^{-2}. This identical potential was applied to all samples. The frequency range was set at 1×10^5 to 0.01 Hz, and the AC amplitude was set at 5 mV. The stability test was performed using the chronopotentiometric method to evaluate the performance of the $NiCo_2O_4$@a-NiFeO(OH) electrode at a constant current density of 100 mA cm^{-2}. To obtain the Faraday efficiency of oxygen (FE_{O2}), chronopotential measurements were carried out on $NiCo_2O_4$@NiFeO(OH) samples at a constant current of 0.25 A for 1397 s. We obtained 20 mL of gas, taking the volume of 1 mol of the ideal gas to be 22.4 L. The FE_{O2} was calculated by the following equation: $n_{theory} = \frac{I \times t}{4 \times F} = \frac{0.25 \times 1397}{4 \times 96485} = 0.000905$ mol, $n_{actual} = \frac{0.02}{22.4} = 0.000893$ mol, $FE_{O2} = \frac{n_{actual}}{n_{theory}} \times 100\% = 98.67\%$. The electrochemical active surface area (ECSA) of $NiCo_2O_4$@a-NiFeO(OH) and its contrasting samples was obtained based on the bilayer capacitance method, and its value was calculated by the equation ECSA = C_{dl}/C_s. In the formula, the specific capacitance (C_s) is a constant 0.040 mF cm^{-2}, and the electrochemical double-layer capacitance (C_{dl}) value was obtained from the CV curves at different sweep speeds, setting sweep speeds of 1, 3, 5, 7, and 9 mV s^{-1} for the CV test.

3. RESULTS AND DISCUSSION

Well-crystallized $NiCo_2O_4$ composite amorphous NiFeO(OH) heterostructures ($NiCo_2O_4$@a-NiFeO(OH)) have been prepared using a hydrothermal process followed by an impregnation treatment (Figure 1). Initially, $NiCo_2O_4$ nanoneedle arrays uniformly grown on NF were fabricated through a hydrothermal reaction and subsequent annealing, providing a robust scaffold for the subsequent growth of amorphous NiFeO(OH). The impregnation of the $NiCo_2O_4$ structure in a NiFe precursor solution, followed by natural air-drying, resulted in the formation of uniformly grown and well-structured $NiCo_2O_4$@a-NiFeO(OH) heterostructured catalysts. Notably, the formation of amorphous NiFeO(OH) on the surface of $NiCo_2O_4$ modulates the microstructure of the amorphous layer, demonstrating the versatility of this preparation method. As a further comparison, $NiCo_2O_4$@a-NiCoO(OH) and $NiCo_2O_4$@a-NiMnO(OH) heterostructured catalysts were also synthesized using the same method. The surface morphology of the $NiCo_2O_4$ sample after the hydrothermal reaction and the sample was heated at 350 °C was observed using a scanning electron microscope (SEM) (Figure S1). The $NiCo_2O_4$ structure exhibited a nanoneedle-like morphology. The surface morphology of $NiCo_2O_4$@a-NiFeO(OH) and its comparative samples was investigated using SEM. SEM images at various magnifications of $NiCo_2O_4$@a-NiMO(OH) (M = Fe, Co, Mn) revealed similar

https://doi.org/10.1021/acs.energyfuels.5c02583
Energy Fuels 2025, 39, 17522−17530

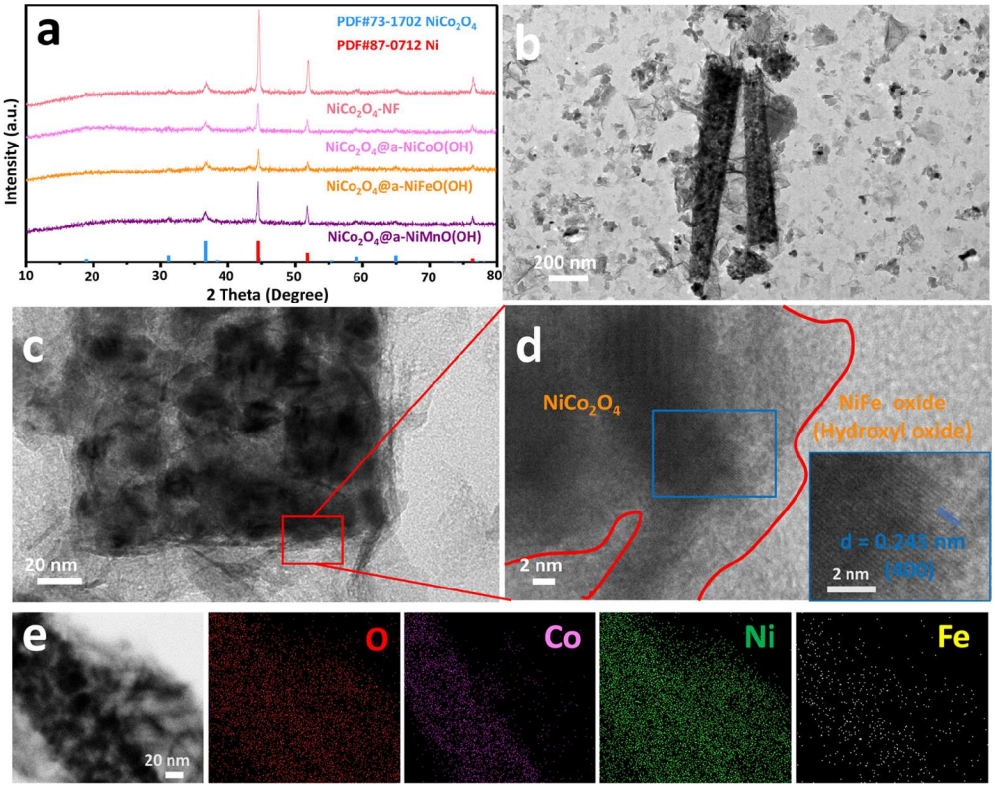

Figure 3. (a) XRD patterns of $NiCo_2O_4$ powder, $NiCo_2O_4$@a-NiCoO(OH), $NiCo_2O_4$@a-NiFeO(OH), and $NiCo_2O_4$@a-NiMnO(OH). (b,c) TEM images and (d) HRTEM image of $NiCo_2O_4$@a-NiFeO(OH); (e) TEM image of $NiCo_2O_4$@a-NiFeO(OH) and the corresponding EDS elemental mapping images.

microstructures across all samples, characterized by uniformly grown two-dimensional nanosheets wrapped around $NiCo_2O_4$ scaffolds (Figure 2). In contrast, SEM images of NiMO(OH) directly grown on NF (NiM-NF, M = Fe, Co, Mn) (Figures S2−S4) show irregular morphologies, comprising spherical, network-like, and bulk formations. Comparison between the two sets of images suggests that the nanoneedle structure of $NiCo_2O_4$ performs a crucial function in facilitating the homogeneous growth of NiMO(OH) nanosheets, indicating the universality of this preparation method to a certain extent.

The crystal structures of $NiCo_2O_4$@a-NiFeO(OH) and its comparison samples were analyzed by XRD, as shown in Figure 3a. The diffraction patterns exhibit the characteristic peaks of the spinel $NiCo_2O_4$ structure (JCPDS No. 73-1702); however, the diffraction peaks are attenuated compared to those of $NiCo_2O_4$−NF, which can be ascribed to the existence of the NiMO(OH) overlayer, which partially obscures the $NiCo_2O_4$ signal. Notably, the dominant peaks at 44.4°, 52.0°, and 76.4° correspond to the NF substrate. No diffraction peaks associated with NiMO(OH) were observed, consistent with the amorphous nature of the NiMO(OH) phase, which is known for its high intrinsic electrocatalytic activity.[31] To further determine the amorphous nature of the structure and the formation of the heterostructure, TEM and high-resolution TEM (HRTEM) were employed. The FTIR images of $NiCo_2O_4$ and $NiCo_2O_4$@a-NiFeO(OH) are shown in Figure S5. The FTIR spectra of $NiCo_2O_4$@a-NiFeO(OH) are shown in Figure S5a, with broad peak shapes and reduced intensity proving the successful synthesis of the amorphous layer, and comparison with $NiCo_2O_4$ reveals that the peaks located at 3300 cm^{-1} correspond to the telescopic vibration of the hydroxyl group of NiFeO(OH), and the peaks at 640 cm^{-1} correspond to the telescopic vibration of the metal−oxygen (Fe−O).[33] The FTIR spectra of $NiCo_2O_4$ in Figure S5b showing that the peaks are located at 3400 cm^{-1} and 1600 cm^{-1} correspond to the O−H stretching vibration and the H−O−H bending vibration of the water molecules adsorbed on the surface of the samples.[34] The TEM images of $NiCo_2O_4$@a-NiFeO(OH) (Figure 3b,c) clearly show the successful deposition of amorphous NiFeO(OH) nanosheets onto the $NiCo_2O_4$ surface, confirming the formation of the composite heterostructure. HRTEM analysis (Figure 3d) reveals the presence of an amorphous−crystalline heterointerface with lattice fringes corresponding to $NiCo_2O_4$ (JCPDS No. 73-1702). Specifically, the lattice spacing of 0.245 nm is attributed to the (400) planes of $NiCo_2O_4$. The right half of the HRTEM image displays a clear amorphous region, consistent with that of the NiFeO(OH) phase. The TEM image and the corresponding elemental mapping of $NiCo_2O_4$@a-NiFeO-(OH) further verify the uniform distribution of Ni, Fe, Co, and O elements, with Co predominantly localized in the $NiCo_2O_4$ nanoneedle structure and Ni and Fe uniformly distributed throughout the amorphous NiFeO(OH) nanosheets, thereby affirming the formation of a well-defined heterogeneous structure (Figure 3e). The HRTEM images of $NiCo_2O_4$@a-NiFeO(OH) and $NiCo_2O_4$ samples were subjected to Fast Fourier Transform (FFT), as shown in Figures S6 and S7. From Figures S6b and S7c, it can be seen that after performing FFT on the HRTEM images of the $NiCo_2O_4$ sample and the internal structure of $NiCo_2O_4$@a-NiFeO(OH), the diffraction rings displayed correspond to the spinel-type $NiCo_2O_4$. This helps to prove the polycrystalline structure of

https://doi.org/10.1021/acs.energyfuels.5c02583
Energy Fuels 2025, 39, 17522−17530

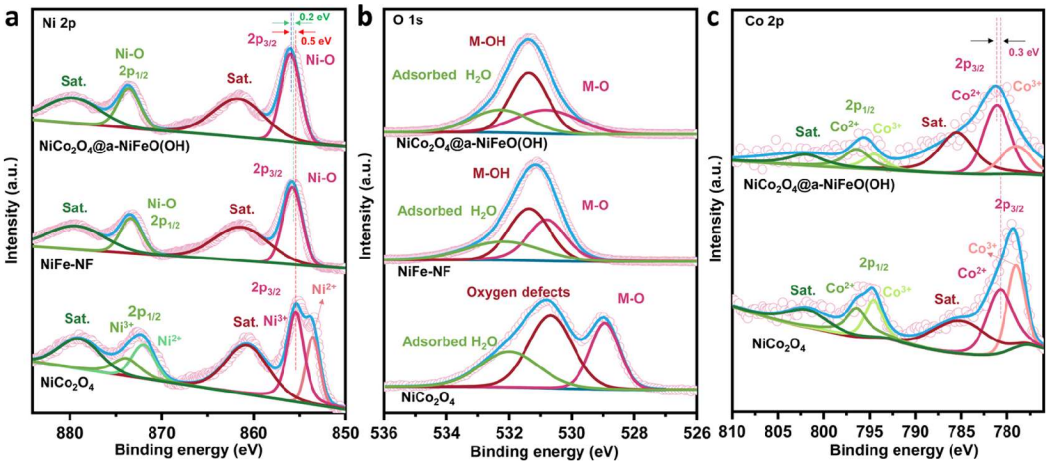

Figure 4. XPS spectra of (a) Ni 2p, (b) O 1s, and (c) Co 2p of $NiCo_2O_4$@a-NiFeO(OH), NiFe-NF, and $NiCo_2O_4$.

the $NiCo_2O_4$. In the lower image of Figure S7c, it is shown that NiFeO(OH) on the surface of $NiCo_2O_4$@a-NiFeO(OH) is amorphous, presenting a diffuse halo. To further confirm the elemental ratios of Ni and Fe in the amorphous NiFeO(OH) nanosheets, point-scan elemental mapping analysis was performed on the amorphous layer of NiFeO(OH). From the elemental distribution spectra, it can be seen that the ratios of Ni to Fe are approximately 1:1 (Figure S8). The EDS elemental mapping images of $NiCo_2O_4$@a-NiFeO(OH) are consistent with the elemental mapping (Figure S9). Notably, the Fe content is lower than expected, despite the 1:1 Fe/Ni feed ratio used during the sample preparation. This discrepancy can be attributed to the high reactivity and corrosivity of Fe^{3+} in the impregnation solution, where it acts as a corrosive and oxidizing agent during the growth of amorphous NiFeO(OH).[35]

A deep understanding of the surface elemental states and electronic configurations of heterostructures is essential to elucidating the synergistic effects of heterostructures. To this end, XPS was performed on $NiCo_2O_4$@a-NiFeO(OH), NiFe-NF, and $NiCo_2O_4$. Figure S10 presents the survey XPS spectra of $NiCo_2O_4$@a-NiFeO(OH) and $NiCo_2O_4$, clearly showing the presence of Ni, O, Co, and Fe in $NiCo_2O_4$@a-NiFeO(OH) and the presence of Ni, O, and Co in $NiCo_2O_4$. Figure 4a,b show the high-resolution XPS spectra of Ni 2p and O 1s, indicating significant changes in the chemical environments of Ni and O in $NiCo_2O_4$@a-NiFeO-(OH) compared to NiFe-NF and $NiCo_2O_4$. The similarity between $NiCo_2O_4$@a-NiFeO(OH) and NiFe-NF in the Ni 2p and O 1s spectra confirms the successful deposition of NiFeO(OH) on the $NiCo_2O_4$ surface, resulting in complete coverage by the amorphous NiFeO(OH). In the Ni 2p spectrum of $NiCo_2O_4$@a-NiFeO(OH), peaks at 855.6 and 873.6 eV are related to Ni^{3+} and Ni−O bonds, while satellite peaks appear at 861.6 and 879.7 eV.[36,37] Notably, a positive shift of 0.5 eV in the Ni $2p_{3/2}$ binding energy relative to $NiCo_2O_4$ and 0.2 eV relative to NiFe-NF suggests electronic interactions between $NiCo_2O_4$ and a-NiFeO(OH), with $NiCo_2O_4$ influencing the electronic structure of a-NiFeO-(OH). This shift, which reflects an increase in the Ni oxidation state, is beneficial for OER.[38,39] In the O 1s spectrum (Figure 4b), peaks at 530.8, 531.36, and 532.27 eV correspond to lattice oxygen, metal hydroxides, and adsorbed oxygen, respectively.[40,41] The stronger M−OH peak intensity in $NiCo_2O_4$@a-NiFeO(OH) compared to NiFe-NF suggests enhanced surface hydroxylation, which aligns with the elevated Ni binding energy and further promotes the OER process. The Co 2p spectra (Figure 4c) reveal a shift in the chemical environment of Co, with peaks at 781.1 and 796.5 eV ascribed to Co^{2+}.[42,43] A shift of 0.3 eV toward higher binding energies in Co $2p_{3/2}$ compared to $NiCo_2O_4$ likely arises from enhanced surface hydroxylation.[44,45] The Fe 2p spectra (Figure S11) exhibit no significant peak shifts, indicating that the Fe valence state remains largely unchanged. Collectively, these results suggest that the synergistic interaction between the $NiCo_2O_4$ and a-NiFeO(OH) phases, along with enhanced surface hydroxylation, leads to increased oxidation states for the Ni and Co species. However, the oxidation state of Fe remains unaffected. It is therefore reasonable to infer that the surface Ni sites in $NiCo_2O_4$@a-NiFeO(OH) serve as the primary active sites for OER. The heterostructure promotes electron transfer and enhances surface hydroxylation, which facilitates the adsorption and desorption of oxygen species during OER, thereby improving the catalytic performance.[46,47]

To evaluate the OER activity of $NiCo_2O_4$@a-NiFeO(OH) and comparison samples, electrochemical tests were carried out by using a standard three-electrode system in 1 M KOH. Figure 5a,b present the LSV curves, and the overpotentials at 10 and 100 mA cm^{-2} are summarized in Table S1. $NiCo_2O_4$@a-NiFeO(OH) exhibited the highest catalytic activity, requiring overpotentials of only 219.6 and 260.8 mV for reaching current densities of 10 mA cm^{-2} and 100 mA cm^{-2}, respectively. Additionally, the OER performance of $NiCo_2O_4$@a-NiMO-(OH) was superior to that of its NiM-NF counterparts. For example, $NiCo_2O_4$@a-NiFeO(OH) (219.6 mV) outperformed NiFe-NF (225.8 mV), $NiCo_2O_4$@a-NiCoO(OH) (276.3 mV) outperformed NiCo-NF (329.7 mV), and $NiCo_2O_4$@a-NiMnO(OH) (296.7 mV) surpassed NiMn-NF (323.2 mV). These results indicate that the heterostructured nanosheet-nanoneedle composites significantly enhance the performance of the OER, primarily due to the synergistic effect of the heterostructure and optimized electronic structure. The FE_{O2} of $NiCo_2O_4$@a-NiFeO(OH) was analyzed by gas chromatography and obtained to be 98.67%, which indicates the excellent catalytic selectivity and charge utilization efficiency (Figure S12). In order to understand the electrochemical behavior of $NiCo_2O_4$@a-NiFeO(OH) and $NiCo_2O_4$, a full-scale CV test was performed (Figure S13). The negative shift in the Co^{3+}

https://doi.org/10.1021/acs.energyfuels.5c02583
Energy Fuels 2025, 39, 17522−17530

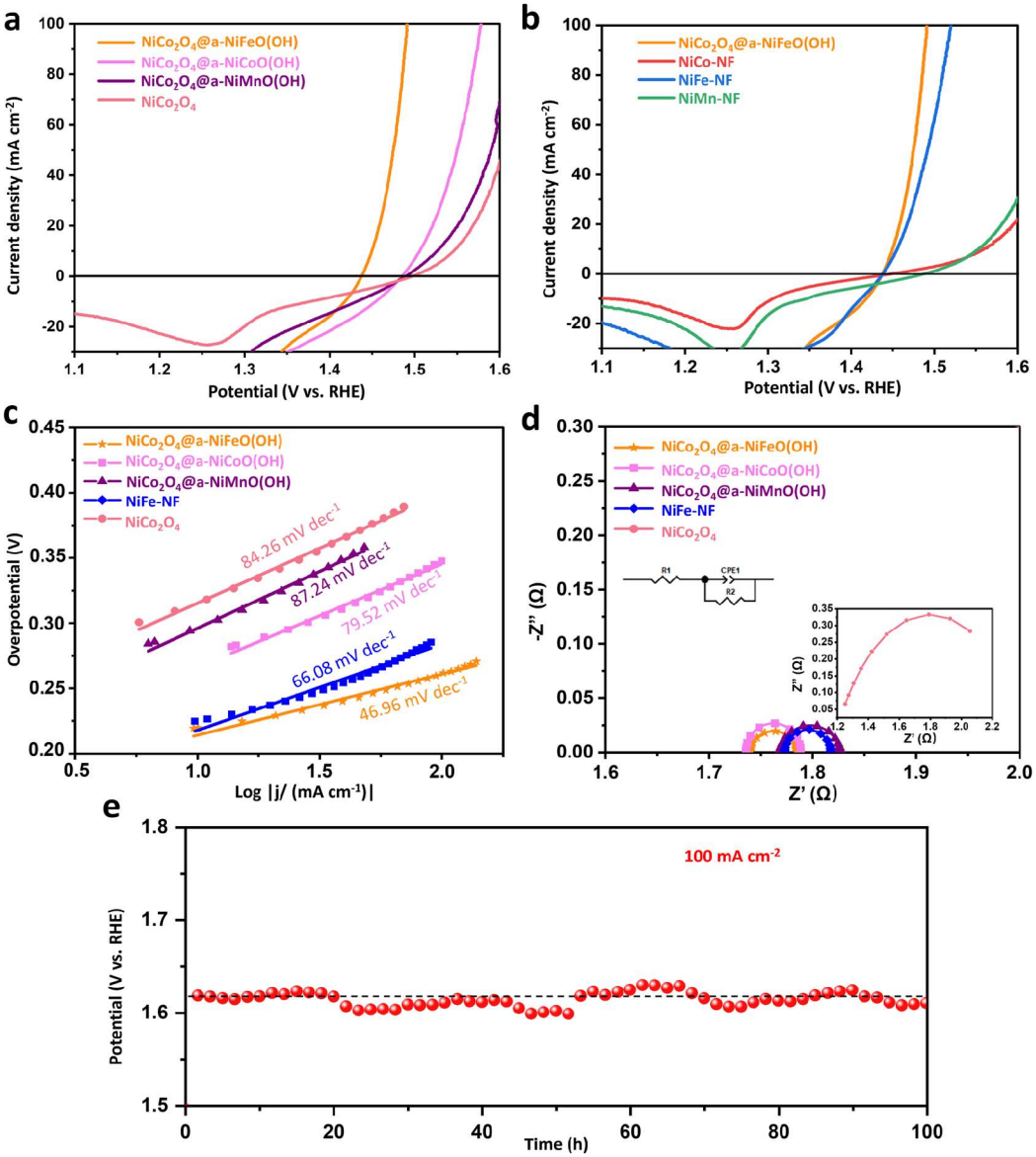

Figure 5. (a) LSV curves of $NiCo_2O_4$@a-NiFeO(OH), $NiCo_2O_4$@a-NiCoO(OH), $NiCo_2O_4$@a-NiMnO(OH), and $NiCo_2O_4$ at a scan of 5 mV s^{-1} in 1 M KOH. (b) LSV curves of $NiCo_2O_4$@a-NiFeO(OH), NiCo-NF, NiFe-NF, and NiMn-NF at a scan of 5 mV s^{-1} in 1 M KOH. (c) Tafel slopes and (d) Nyquist plots of $NiCo_2O_4$@a-NiFeO(OH), $NiCo_2O_4$@a-NiCoO(OH), $NiCo_2O_4$@a-NiMnO(OH), NiFe-NF, and $NiCo_2O_4$. The inset shows Nyquist plots of $NiCo_2O_4$. (e) Chronopotentiometric curve of the $NiCo_2O_4$@a-NiFeO(OH) under a constant current density of 100 mA cm^{-2}.

oxidation peak potential observed for $NiCo_2O_4$@a-NiFeO-(OH) relative to pristine $NiCo_2O_4$ signifies critical structural and electronic modifications induced by the integration of NiFeOOH. On the one hand, the lower oxidation potential implies a reduced energy barrier for the Co^{3+} oxidation process, indicating enhanced catalytic kinetics for the $NiCo_2O_4$@a-NiFeO(OH). On the other hand, the interfacial electronic interactions between $NiCo_2O_4$ and NiFeOOH induce synergistic charge redistribution, altering the local electronic environment of Co^{3+} and promoting their oxidation at a lower overpotential. Moreover, the negative potential shift correlates with a reduced overpotential and improved electron-transfer kinetics for the OER, suggesting that the $NiCo_2O_4$@a-NiFeO(OH) composite exhibits superior efficiency in the OER processes compared to $NiCo_2O_4$. Tafel slope analysis (Figure 5c) revealed that $NiCo_2O_4$@a-NiFeO(OH) exhibited the lowest Tafel slope (46.96 mV dec^{-1}), suggesting improved OER kinetics compared with the other samples. EIS data (Figure 5d) demonstrated that $NiCo_2O_4$@a-NiFeO(OH) has the lowest charge transfer resistance (R_{ct}), further confirming its superior electron transfer capabilities. Besides the assessment of catalytic activity, electrochemical stability is also a significant parameter for evaluating the performance of materials, which is regarded as being very important in practical production applications. Chronopotentiometry testing (Figure 5e) showed that $NiCo_2O_4$@a-NiFeO(OH) remains stable at a current density of 100 mA cm^{-2} for 100 h, indicating excellent electrochemical stability. The electrochemical analyses presented above indicate that $NiCo_2O_4$@a-NiFeO(OH) exhibits optimized OER properties, primarily driven by the synergistic interaction between crystalline $NiCo_2O_4$ and amorphous NiFeO(OH). The nanosheet

https://doi.org/10.1021/acs.energyfuels.5c02583
Energy Fuels 2025, 39, 17522−17530

morphology of NiFeO(OH) offers a greater density of exposed active sites compared to the morphologically disordered NiFe-NF. This composite heterostructure strategy has proven to be highly effective in significantly enhancing the OER activity of the materials.

To better characterize the intrinsic catalytic activity of the materials, the LSV curves of different samples were normalized by ECSA. The CV of $NiCo_2O_4$@a-NiFeO(OH), $NiCo_2O_4$@a-NiCoO(OH), $NiCo_2O_4$@a-NiMnO(OH), and $NiCo_2O_4$ was tested in the non-Faraday interval from 0.832 to 0.932 V vs RHE, and the C_{dl} values of the samples were obtained by calculation (Figures S14 and S15). Figure S16 shows the ECSA normalized LSV curves of different samples, through which it can be found that $NiCo_2O_4$@a-NiFeO(OH) has the highest intrinsic catalytic efficiency.

To further assess the structural stability of $NiCo_2O_4$@a-NiFeO(OH), the material after the reaction was characterized using SEM, TEM, and EDS. The SEM images of $NiCo_2O_4$@a-NiFeO(OH) at various magnifications, following 2 h of reaction at a current density of 100 mA cm^{-2} (Figure S17), reveal that its one-dimensional nanoneedle and two-dimensional nanosheet composite structure remained fully intact. TEM analysis (Figure S18) further confirms that the amorphous NiFeO(OH) completely encapsulates $NiCo_2O_4$ postreaction, and the interface heterostructure remains well-preserved, as evidenced by HRTEM images. Additionally, EDS elemental mapping (Figure S19) demonstrates that O, Ni, and Fe remain uniformly distributed throughout the material, while Co remains concentrated in the central region, further confirming the structural integrity of the composite heterostructure.

4. CONCLUSION

In summary, a heterostructured material of the crystalline $NiCo_2O_4$ composite amorphous NiFeO(OH) ($NiCo_2O_4$@a-NiFeO(OH)) has been prepared by hydrothermal and impregnation treatment. The obtained $NiCo_2O_4$@a-NiFeO-(OH) exhibited an enhanced OER catalytic activity, which is attributed to the heterostructure that leads to the electron transfer between the two phases, resulting in the elevation of the valence state of the Ni species and also the enhancement of the surface hydroxylation, which results in the material having more hydroxyl oxides on the surface as the active sites, facilitating the adsorption/resolution process of the O species for the OER process and boosting the OER process. Consequently, only 219.6 and 260.8 mV of overpotentials are needed at current densities of 10 and 100 mA cm^{-2}, respectively. The synergistic effects and optimized electronic interactions within the heterostructure provide a promising pathway for improving catalytic efficiency, underscoring the value of such strategies in the development of advanced electrocatalysts.

■ ASSOCIATED CONTENT

Supporting Information

The Supporting Information is available free of charge at https://pubs.acs.org/doi/10.1021/acs.energyfuels.5c02583.

SEM images of precursors and comparison samples; FTIR, HRTEM, FFT, point-scan EDS mapping, TEM−EDS, survey XPS spectra, and high-resolution XPS spectra images of catalysts; GC images of experimental samples for Faraday efficiency tests; CV images of catalysts at different sweep rates; plots of double-layer capacitor charging current density versus CV scan rate; LSV images of catalysts after ECSA normalization; SEM, TEM, HRTEM, and TEM−EDS images of the catalyst after the reaction; and overpotential graphs of all the samples at different current densities (PDF)

■ AUTHOR INFORMATION

Corresponding Authors

Xin Yu Zhang − *Department of Energy and Chemical Engineering, School of Resources and Environmental Engineering and Engineering Research Center of Resource Utilization of Carbon-containing Waste with Carbon Neutrality, Ministry of Education, East China University of Science and Technology, Shanghai 200237, China*; Email: xy_zhang@ecust.edu.cn

Peng Fei Liu − *Key Laboratory for Ultrafine Materials of Ministry of Education, Shanghai Engineering Research Center of Hierarchical Nanomaterials, School of Materials Science and Engineering, East China University of Science and Technology, Shanghai 200237, China; Engineering Research Center of Resource Utilization of Carbon-containing Waste with Carbon Neutrality, Ministry of Education, East China University of Science and Technology, Shanghai 200237, China*; orcid.org/0000-0003-0411-0488; Email: pfliu@ecust.edu.cn

Authors

Jia Heng Leng − *Key Laboratory for Ultrafine Materials of Ministry of Education, Shanghai Engineering Research Center of Hierarchical Nanomaterials, School of Materials Science and Engineering, East China University of Science and Technology, Shanghai 200237, China*

Zeng Guo Wang − *Key Laboratory for Ultrafine Materials of Ministry of Education, Shanghai Engineering Research Center of Hierarchical Nanomaterials, School of Materials Science and Engineering, East China University of Science and Technology, Shanghai 200237, China*

Xiaoxia Li − *China General Nuclear New Energy Holdings Co., Ltd., Beijing 100071, China*

Zhaoliang Wang − *Key Laboratory for Ultrafine Materials of Ministry of Education, Shanghai Engineering Research Center of Hierarchical Nanomaterials, School of Materials Science and Engineering, East China University of Science and Technology, Shanghai 200237, China*

Ji Kai Liu − *Key Laboratory for Ultrafine Materials of Ministry of Education, Shanghai Engineering Research Center of Hierarchical Nanomaterials, School of Materials Science and Engineering, East China University of Science and Technology, Shanghai 200237, China*

Hua Gui Yang − *Key Laboratory for Ultrafine Materials of Ministry of Education, Shanghai Engineering Research Center of Hierarchical Nanomaterials, School of Materials Science and Engineering, East China University of Science and Technology, Shanghai 200237, China; Engineering Research Center of Resource Utilization of Carbon-containing Waste with Carbon Neutrality, Ministry of Education, East China University of Science and Technology, Shanghai 200237, China*; orcid.org/0000-0003-0436-8622

Complete contact information is available at: https://pubs.acs.org/10.1021/acs.energyfuels.5c02583

Author Contributions

The manuscript was written through the contributions of all authors. All authors have approved the final version of the manuscript.

Notes

The authors declare no competing financial interest.

■ ACKNOWLEDGMENTS

This work was financially supported by the National Natural Science Foundation of China (22309053) and the Science and Technology Commission of Shanghai Municipality (23YF1408500).

■ REFERENCES

(1) Armaroli, N.; Balzani, V. The future of energy supply: challenges and opportunities. *Angew. Chem., Int. Ed.* **2007**, *46* (1−2), 52−66.
(2) Al, S. COP28: the science is clear- fossil fuels must go. *Nature* **2023**, *624*, 225.
(3) Yu, Z. Y.; Duan, Y.; Feng, X. Y.; Yu, X.; Gao, M. R.; Yu, S. H. Clean and Affordable Hydrogen Fuel from Alkaline Water Splitting: Past, Recent Progress, and Future Prospects. *Adv. Mater.* **2021**, *33* (31), 2007100.
(4) Huang, H.; Yan, M.; Yang, C.; He, H.; Jiang, Q.; Yang, L.; Lu, Z.; Sun, Z.; Xu, X.; Bando, Y.; et al. Graphene nanoarchitectonics: recent advances in graphene-based electrocatalysts for hydrogen evolution reaction. *Adv. Mater.* **2019**, *31* (48), 1903415.
(5) Jiang, Y.; Liang, Z.; Fu, H.; Sun, M.; Wang, S.; Huang, B.; Du, Y. Pt-Modified High Entropy Rare Earth Oxide for Efficient Hydrogen Evolution in pH-Universal Environments. *J. Am. Chem. Soc.* **2024**, *146* (13), 9012−9025.
(6) Yu, M.; Budiyanto, E.; Tüysüz, H. Principles of water electrolysis and recent progress in cobalt-nickel-and iron-based oxides for the oxygen evolution reaction. *Angew. Chem., Int. Ed.* **2022**, *61* (1), No. e202103824.
(7) Greeley, J.; Markovic, N. M. The road from animal electricity to green energy: combining experiment and theory in electrocatalysis. *Energy Environ. Sci.* **2012**, *5* (11), 9246−9256.
(8) Martín, A. J.; Pérez-Ramírez, J. Heading to distributed electrocatalytic conversion of small abundant molecules into fuels, chemicals, and fertilizers. *Joule* **2019**, *3* (11), 2602−2621.
(9) Xue, H.; Yang, T.; Zhang, Z.; Zhang, Y.; Geng, Z.; He, Y. Stimulate the hidden catalysis potential and exposure of nickel site in NiSe@CNTs result in ultra-high HER/OER activity and stability. *Appl. Catal., B* **2023**, *330*, 122641.
(10) Zhang, B.; Zheng, X.; Voznyy, O.; Comin, R.; Bajdich, M.; García-Melchor, M.; Han, L.; Xu, J.; Liu, M.; Zheng, L.; et al. Homogeneously dispersed multimetal oxygen-evolving catalysts. *Science* **2016**, *352* (6283), 333−337.
(11) Zhao, Y.; Lu, X. F.; Fan, G.; Luan, D.; Gu, X.; Lou, X. W. Surface-exposed single-Ni atoms with potential-driven dynamic behaviors for highly efficient electrocatalytic oxygen evolution. *Angew. Chem., Int. Ed.* **2022**, *61* (45), No. e202212542.
(12) Bi, S.; Geng, Z.; Wang, Y.; Gao, Z.; Jin, L.; Xue, M.; Zhang, C. Multi-Stage Porous Nickel-Iron Oxide Electrode for High Current Alkaline Water Electrolysis. *Adv. Funct. Mater.* **2023**, *33* (31), 2214792.
(13) Le Formal, F.; Yerly, L.; Mensi, E. P.; Da Costa, X. P.; Boudoire, F.; Guijarro, N.; Spodaryk, M.; Züttel, A.; Sivula, K. Influence of composition on performance in metallic iron−nickel−cobalt ternary anodes for alkaline water electrolysis. *ACS Catal.* **2020**, *10* (20), 12139−12147.
(14) Liu, X.; Wang, X.; Yuan, X.; Dong, W.; Huang, F. Rational composition and structural design of in situ grown nickel-based electrocatalysts for efficient water electrolysis. *J. Mater. Chem. A* **2016**, *4* (1), 167−172.
(15) Vij, V.; Sultan, S.; Harzandi, A. M.; Meena, A.; Tiwari, J. N.; Lee, W.-G.; Yoon, T.; Kim, K. S. Nickel-based electrocatalysts for energy-related applications: oxygen reduction, oxygen evolution, and hydrogen evolution reactions. *ACS Catal.* **2017**, *7* (10), 7196−7225.
(16) Chakthranont, P.; Kibsgaard, J.; Gallo, A.; Park, J.; Mitani, M.; Sokaras, D.; Kroll, T.; Sinclair, R.; Mogensen, M. B.; Jaramillo, T. F. Effects of gold substrates on the intrinsic and extrinsic activity of high-loading nickel-based oxyhydroxide oxygen evolution catalysts. *ACS Catal.* **2017**, *7* (8), 5399−5409.
(17) Oshchepkov, A. G.; Braesch, G.; Bonnefont, A.; Savinova, E. R.; Chatenet, M. Recent advances in the understanding of nickel-based catalysts for the oxidation of hydrogen-containing fuels in alkaline media. *ACS Catal.* **2020**, *10* (13), 7043−7068.
(18) Wang, J.; Gao, Y.; Kong, H.; Kim, J.; Choi, S.; Ciucci, F.; Hao, Y.; Yang, S.; Shao, Z.; Lim, J. Non-precious-metal catalysts for alkaline water electrolysis: operando characterizations, theoretical calculations, and recent advances. *Chem. Soc. Rev.* **2020**, *49* (24), 9154−9196.
(19) Yang, H.; Driess, M.; Menezes, P. W. Self-supported electrocatalysts for practical water electrolysis. *Adv. Energy Mater.* **2021**, *11* (39), 2102074.
(20) Zhang, X. Y.; Lou, Z. X.; Chen, J.; Liu, Y.; Wu, X.; Zhao, J. Y.; Yuan, H. Y.; Zhu, M.; Dai, S.; Wang, H. F.; et al. Direct OC-CHO coupling towards highly C_{2+} products selective electroreduction over stable Cu^0/Cu^{2+} interface. *Nat. Commun.* **2023**, *14*, 7681.
(21) Fu, H. Q.; Zhou, M.; Liu, P. F.; Liu, P.; Yin, H.; Sun, K. Z.; Yang, H. G.; Al-Mamun, M.; Hu, P.; Wang, H.-F.; et al. Hydrogen spillover-bridged Volmer/Tafel processes enabling ampere-level current density alkaline hydrogen evolution reaction under low overpotential. *J. Am. Chem. Soc.* **2022**, *144* (13), 6028−6039.
(22) Huang, Q.; Xia, G.-J.; Huang, B.; Xie, D.; Wang, J.; Wen, D.; Lin, D.; Xu, C.; Gao, L.; Wu, Z.; et al. Activating lattice oxygen by a defect-engineered Fe_2O_3-CeO_2 nano-heterojunction for efficient electrochemical water oxidation. *Energy Environ. Sci.* **2024**, *17* (14), 5260−5272.
(23) Hu, L.; Zeng, X.; Wei, X.; Wang, H.; Wu, Y.; Gu, W.; Shi, L.; Zhu, C. Interface engineering for enhancing electrocatalytic oxygen evolution of NiFe LDH/NiTe heterostructures. *Appl. Catal., B* **2020**, *273*, 119014.
(24) Liu, J.; Yang, X.; Si, F.; Zhao, B.; Xi, X.; Wang, L.; Zhang, J.; Fu, X.-Z.; Luo, J.-L. Interfacial component coupling effects towards precise heterostructure design for efficient electrocatalytic water splitting. *Nano Energy* **2022**, *103*, 107753.
(25) Ding, H.; Liu, H.; Chu, W.; Wu, C.; Xie, Y. Structural transformation of heterogeneous materials for electrocatalytic oxygen evolution reaction. *Chem. Rev.* **2021**, *121* (21), 13174−13212.
(26) Mann, D. S.; Kwon, S.-N.; Patil, P.; Na, S.-I. Revivification of nickel oxide-perovskite interfaces via nickel nitrate to boost performance in perovskite solar cells. *Nano Energy* **2023**, *106*, 108062.
(27) Guo, S.; Han, S.; Mao, H.; Dong, S.; Wu, C.; Jia, L.; Chi, B.; Pu, J.; Li, J. Structurally controlled ZnO/TiO_2 heterostructures as efficient photocatalysts for hydrogen generation from water without noble metals: The role of microporous amorphous/crystalline composite structure. *J. Power Sources* **2014**, *245*, 979−985.
(28) Zhang, Y.; Gao, F.; Wang, D.; Li, Z.; Wang, X.; Wang, C.; Zhang, K.; Du, Y. Amorphous/crystalline heterostructure transition-metal-based catalysts for high-performance water splitting. *Coord. Chem. Rev.* **2023**, *475*, 214916.
(29) Liu, J.; Qian, G.; Yu, T.; Chen, J.; Zhu, C.; Li, Y.; He, J.; Luo, L.; Yin, S. Amorphous-crystalline heterostructure for simulated practical water splitting at high-current-density. *Chem. Eng. J.* **2022**, *431*, 134247.
(30) Zhang, L.; Wu, Y.; Li, J.; Jin, Z.; Li, Y.; Tsubaki, N. Amorphous/crystalline heterojunction interface driving the spatial separation of charge carriers for efficient photocatalytic hydrogen evolution. *Mater. Today Phys.* **2022**, *27*, 100767.
(31) Yang, Y.; Zhu, B.; Guo, P.-F.; Wang, W.-J.; Wang, W.-T.; Wang, K.; He, Z.-H.; Liu, Z.-T. Core-shell trimetallic NiFeV disulfides and amorphous high-valence NiFe hydroxide nanosheets enhancing oxygen evolution reaction. *Chem. Eng. J.* **2022**, *430*, 133047.
(32) Gong, Z.; Liu, R.; Gong, H.; Ye, G.; Liu, J.; Dong, J.; Liao, J.; Yan, M.; Liu, J.; Huang, K.; et al. Constructing a graphene-

https://doi.org/10.1021/acs.energyfuels.5c02583
Energy Fuels 2025, 39, 17522−17530

encapsulated amorphous/crystalline heterophase NiFe alloy by microwave thermal shock for boosting the oxygen evolution reaction. *ACS Catal.* **2021**, *11* (19), 12284−12292.
(33) Chubar, N.; Gerda, V.; Szlachta, M.; Yablokova, G. Effect of Fe oxidation state (+2 versus + 3) in precursor on the structure of Fe oxides/carbonates-based composites examined by XPS, FTIR and EXAFS. *Solid State Sci.* **2021**, *121*, 106752.
(34) Noor, S.; Sajjad, S.; Leghari, S. A. K.; Long, M. Energy harvesting for electrochemical OER and solar photocatalysis via dual functional GO/TiO_2-NiO nanocomposite. *J. Clean. Prod.* **2020**, *277*, 123280.
(35) Zhao, W.; Xu, H.; Luan, H.; Chen, N.; Gong, P.; Yao, K.; Shen, Y.; Shao, Y. NiFe layered double hydroxides grown on a corrosion-cell cathode for oxygen evolution electrocatalysis. *Adv. Energy Mater.* **2022**, *12* (2), 2102372.
(36) Sun, F.; Wang, G.; Ding, Y.; Wang, C.; Yuan, B.; Lin, Y. NiFe-based metal-organic framework nanosheets directly supported on nickel foam acting as robust electrodes for electrochemical oxygen evolution reaction. *Adv. Energy Mater.* **2018**, *8* (21), 1800584.
(37) Zhang, J.; Wu, D.; Wei, A.; Zhao, Y.; Liu, J.; He, Y.; Liu, Z. Engineering bimetallic cactus-like NiFeOOH/$CoNiSe_2$ heterostructure nanosheets for efficient oxygen evolution and overall water splitting. *Int. J. Hydrogen Energy* **2023**, *48* (74), 28769−28779.
(38) Gamal, S.; Kospa, D. A.; Gebreil, A.; El-Hakam, S.; Ahmed, A. I.; Ibrahim, A. A. $NiCo_2O_4$ spinel supported N-dopped porous Hollow carbon derived MOF functionalized SiO_2 for efficient ORR electrocatalysis. *Int. J. Hydrogen Energy* **2023**, *48* (49), 18890−18905.
(39) Wang, M.; Feng, X.; Li, S.; Ma, Y.; Peng, Y.; Yang, S.; Liu, Y.; Lei, H.; Dang, J.; Zhang, W.; et al. Spinel-type metal oxides with tailored amorphous/crystalline heterointerfaces for enhanced electrocatalytic water splitting. *Adv. Funct. Mater.* **2024**, *34* (51), 2410439.
(40) Chen, W.; Shi, J.; Wu, Y.; Jiang, Y.; Huang, Y. C.; Zhou, W.; Liu, J.; Dong, C. L.; Zou, Y.; Wang, S. Vacancy-induced catalytic mechanism for alcohol electrooxidation on nickel-based electrocatalyst. *Angew. Chem.* **2024**, *136* (4), No. e202316449.
(41) Zhu, B.; Dong, B.; Wang, F.; Yang, Q.; He, Y.; Zhang, C.; Jin, P.; Feng, L. Unraveling a bifunctional mechanism for methanol-to-formate electro-oxidation on nickel-based hydroxides. *Nat. Commun.* **2023**, *14*, 1686.
(42) Guo, S.; Ma, M.; Ge, R.; Algadi, H.; Shao, Q. Hierarchical copper oxide@nickel-cobalt layered double hydroxide for efficient 5-hydroxymethylfurfural electro-oxidation in alkaline seawater. *Adv. Compos. Hybrid Mater.* **2023**, *6* (5), 158.
(43) Liu, W.; Xie, J.; Guo, Y.; Lou, S.; Gao, L.; Tang, B. Sulfurization-induced edge amorphization in copper-nickel-cobalt layered double hydroxide nanosheets promoting hydrazine electrooxidation. *J. Mater. Chem. A* **2019**, *7* (42), 24437−24444.
(44) Hao, Y.; Xu, Y.; Liu, J.; Sun, X. Nickel−cobalt oxides supported on Co/N decorated graphene as an excellent bifunctional oxygen catalyst. *J. Mater. Chem. A* **2017**, *5* (11), 5594−5600.
(45) Qiu, B.; Cai, L.; Wang, Y.; Lin, Z.; Zuo, Y.; Wang, M.; Chai, Y. Fabrication of nickel-cobalt bimetal phosphide nanocages for enhanced oxygen evolution catalysis. *Adv. Funct. Mater.* **2018**, *28* (17), 1706008.
(46) Yang, C.; Ling, W.; Zhu, Y.; Yang, Y.; Dong, S.; Wu, C.; Wang, Z.; Yang, S.; Li, J.; Wang, G.; et al. Surface hydroxylation engineering to boost oxygen evolution reaction on IrO_2/TiO_2 for PEM water electrolyzer. *Appl. Catal., B* **2024**, *358*, 124462.
(47) Shen, Y.; Zhang, X.-L.; Qu, M.-R.; Ma, J.; Zhu, S.; Min, Y.-L.; Gao, M.-R.; Yu, S.-H. Cr dopant mediates hydroxyl spillover on RuO_2 for high-efficiency proton exchange membrane electrolysis. *Nat. Commun.* **2024**, *15*, 7861.

https://doi.org/10.1021/acs.energyfuels.5c02583
Energy Fuels 2025, 39, 17522−17530